

1 **Molecular organization of soluble type III secretion system sorting**
2 **platform complexes**

3 *Ivonne Bernal^{a,b,†}, Jonathan Börnicke^{a,b,†}, Johannes Heidemann^{c,†}, Dmitri*
4 *Svergun^d, Anne Tuukkanen^{d,#}, Charlotte Uetrecht^{c,e,#}, Michael Kolbe^{a,b,f,#}*

5 ^a Center for Structural Systems Biology, Helmholtz Centre for Infection Research, Department of
6 Structural Infection Biology, Notkestraße 85, 22607 Hamburg, Germany

7 ^b Max Planck Institute for Infection Biology, Structural Systems Biology Group, Charitéplatz 1,
8 10117 Berlin, Germany

9 ^c Heinrich Pette Institute, Leibniz Institute for Experimental Virology, Martinstraße 52, 20521
10 Hamburg, Germany

11 ^d European Molecular Biology Laboratory, Hamburg Outstation, Notkestraße 85, 22607
12 Hamburg, Germany

13 ^e European XFEL GmbH, Sample Environment Group, Holzkoppel 4, 22869 Schenefeld,
14 Germany

15 ^f Faculty of Mathematics, Informatics and Natural Sciences, University of Hamburg,
16 Rothenbaumchaussee 19, 20148 Hamburg, Germany

17 [†] these authors contributed equally to this work

18

19 **Running Title: Building Blocks of the *Salmonella* Sorting Platform**

20

21 # Correspondence to: Michael Kolbe, michael.kolbe@helmholtz-hzi.de

22 Center for Structural Systems Biology, Department for Structural Infection Biology, Notkestraße
23 85, 22607 Hamburg, Germany

24 Tel: +49 40 8998 87550

25 Fax: +49 40 8998 2720

26 or

27 Charlotte Uetrecht, charlotte.uetrecht@xfel.eu

28 Heinrich Pette Institute, Leibniz Institute for Experimental Virology, Martinstraße 52, 20521
29 Hamburg, Germany

30 Tel: +49 40 480 51 261

31 Fax: +49 40 480 51 252

32 or

33 Anne Tuukkanen, anne.tuukkanen@embl-hamburg.de

34 European Molecular Biology Laboratory, Hamburg Outstation, Notkestraße 85, Hamburg 22607,
35 Germany

36 Tel: +49 40 89902 113

37 Fax: +49 40 89902 149

38

39

40 **Abstract**

41 Many medically relevant Gram-negative bacteria use the type III secretion system (T3SS) to
42 translocate effector proteins into the host for their invasion and intracellular survival. A multi-
43 protein complex located at the cytosolic interface of the T3SS is proposed to act as a sorting
44 platform by selecting and targeting substrates for secretion through the system. However, the
45 precise stoichiometry and 3D organization of the sorting platform components is unknown. Here
46 we reconstitute soluble complexes of the *Salmonella* Typhimurium sorting platform proteins
47 including the ATPase InvC, the regulator OrgB, the protein SpaO and a recently identified
48 subunit SpaO_C, which we show to be essential for the solubility of SpaO. We establish domain-
49 domain interactions, determine for the first time the stoichiometry of each subunit within the
50 complexes by native mass spectrometry and gain insight into their organization using small-angle
51 X-ray scattering. Importantly, we find that in solution the assembly of SpaO/SpaO_C/OrgB/InvC
52 adopts an extended L-shaped conformation resembling the sorting platform pods seen in *in situ*
53 cryo-electron tomography, proposing that this complex is the core building block that can be
54 conceivably assembled into higher oligomers to form the T3SS sorting platform. The determined
55 molecular arrangements of the soluble complexes of the sorting platform provide important
56 insights into its architecture and assembly.

57 **Introduction**

58 Type III secretion systems (T3SS) are protein nanomachines used by several medically relevant
59 pathogenic Gram-negative bacteria to deliver effector molecules into host cells to subvert
60 multiple cellular processes, leading to diseases such as salmonellosis, bubonic plague or sexually
61 transmitted infections (1,2). The T3SS forms a syringe-shaped macromolecular complex of
62 ~3.5 MDa, whose main elements are a basal body that spans both bacterial membranes and a
63 protruding needle that forms a continuous secretion channel connecting the bacterial and host cell
64 cytoplasm (3-5). The precise assembly and function of the T3SS critically depends on the
65 hierarchical delivery of structural proteins to build the extracellular needle, followed by effector
66 proteins for translocation into the host cell (6,7). The control of this ordered process involves a
67 multi-protein complex associated with the cytoplasmic side of the T3SS that is proposed to act as
68 a sorting platform by recognizing and selecting substrates for secretion through the system (8,9).

69 In *Salmonella* Typhimurium, the components of the sorting platform of the SPI-1 (*Salmonella*
70 pathogenicity island 1) T3SS include the ATPase InvC (SctN in unified nomenclature), the
71 protein SpaO (SctQ), the ATPase regulator OrgB (SctL) and the accessory protein OrgA (SctK)
72 (8). Visualization of the SPI-1 sorting platform by cryo-electron tomographic analysis (CET)
73 indicates that it adopts a structure of six pods containing SpaO that are connected to the T3SS
74 base through OrgA and to a presumed hexameric ATPase through OrgB linkers (10,11).
75 However, this contrasts with other studies on both the *S. Typhimurium* SPI-1 and the *Yersinia*
76 *enterocolitica* T3SS showing the presence of ~24 and ~22 subunits, respectively, of the SctQ
77 protein at the needle base, which suggests a more extensive structure comparable to the
78 continuous cytosolic ring of flagellar T3SSs (12,13). Furthermore, the sorting platform has been
79 found to be a dynamic structure in which different components are exchanging between a T3SS-
80 associated state and a cytosolic pool (12-14).

81 The probably best characterized component in the *Salmonella* SPI-I sorting platform is the
82 protein SpaO. SpaO contains two surface presentation of antigen domains (SPOA1 and SPOA2)
83 that can form SPOA2-SPOA2 homodimers, as well as SPOA1-SPOA2 heterodimers that are able
84 to interact with OrgB (15). Similar to the homologs of other pathogenic bacteria including
85 *Yersinia* and *Shigella* species, the gene encoding SpaO contains an internal translation initiation
86 site and produces an additional short isoform comprising the SPOA2 domain of SpaO, which we

87 refer to as SpaO_C (16,17). This short product interacts with the full-length protein in other species
88 and thus could represent an additional structural component of the sorting platform (12,18-20).
89 However, the function of SpaO_C in type III secretion is elusive, and how it interacts with the
90 other subunits of the sorting platform is unknown. Moreover, the precise protein composition and
91 spatial molecular organization of the sorting platform, as well its assembly process and
92 mechanism of action in substrate sorting remain uncertain.

93 In this study, we reconstitute and analyze for the first time the soluble assembling units of the
94 *Salmonella* Typhimurium SPI-1 sorting platform using purified proteins. We observe that SpaO_C,
95 the second protein product of the gene *spaO*, is required for fully efficient type III function and
96 for the stability of the sorting platform complexes in solution. Using native mass spectrometry
97 (MS), small-angle X-ray scattering (SAXS) and multi-angle light scattering (MALS), we
98 characterize different substructures of the sorting platform, determining their stoichiometry and
99 association into SpaO/SpaO_C/OrgB/InvC complexes. These complexes adopt an extended L-
100 shaped conformation in solution that mirrors a segment of the sorting platform visualized by
101 CET. Our data present the most detailed assembly of the *Salmonella* Typhimurium SPI-1 sorting
102 platform in solution, reporting the conformation of what we propose is the core building block to
103 assemble the sorting platform at the T3SS needle base.

104

105

106 **Results**

107

108 **The *spaO* gene encodes two protein products required for fully active type III secretion.**
109 SpaO is a critical component of the *S. Typhimurium* SPI-1 sorting platform and it has recently
110 been shown that the *spaO* gene, similar to several of its homologs in other T3SSs, produces both
111 the full-length SpaO protein and a shorter variant that is the result of translation initiation from an
112 internal ribosome binding site (RBS) (17). When we recombinantly expressed C-terminally
113 *Strep*-tagged *spaO* and purified the protein by *Strep*-Tactin affinity purification, we could
114 confirm the production of this smaller protein product SpaO_C (Fig. 1A). Using MALDI MS and
115 Edman sequencing we found that it begins with a methionine, rather than a valine that is encoded

116 at its starting position at codon 203 (Fig. S1 and Table S1), supporting the conclusion that it is the
117 product of internal translation initiation.

118
119 To examine the role of the SpaO isoforms in the infection process of *S. Typhimurium*, we first
120 created mutants that produce only the full-length or short variant of SpaO by introducing into the
121 chromosome either two stop codons shortly after the *spaO* start codon ($\Delta spaO_{FL}$) or silent
122 mutations in both the putative RBS and start codon of SpaO_C ($\Delta spaO_C$) (Fig. 1A). We tested the
123 ability of these mutants to secrete T3SS substrate proteins into the culture supernatant, which
124 showed that loss of SpaO_{FL} causes complete inhibition of T3SS function similar to that observed
125 for *spaO* gene knockout mutants (Fig. 1B). In contrast, abrogation of SpaO_C translation resulted
126 in a marked reduction in secretion, which could almost completely be restored by
127 complementation with *spaO_C*. Similarly, while the deletion of SpaO completely abolished the
128 ability of *Salmonella* to invade host cells, loss of SpaO_C resulted in a statistically significant
129 reduction of invasiveness by about 50% compared to the wild type (Fig. 1C). However, it is
130 possible that the loss of SpaO_C in the $\Delta spaO_C$ mutant is incomplete, because when we expressed
131 and affinity-purified a SpaO variant in which only the start codon of SpaO_C was mutated from
132 GTG to GCG (SpaO_{V203A}), small amounts of SpaO_C were still co-purified with the full-length
133 SpaO (Fig. 2A). MALDI MS of this SpaO_C showed the presence of both methionine and alanine
134 in the first amino acid position (Fig. S2, Table S2), indicating that even in the absence of internal
135 translation initiation a SpaO_C-like protein can still be produced by an alternative mechanism,
136 probably proteolysis.

137
138 **SpaO_C dimers bind to the N-terminal domain of SpaO to form SpaO-2SpaO_C complexes.** In
139 order to determine the molecular function of SpaO_C in type III secretion, we first tested the
140 influence of SpaO_C on SpaO stability. To this end, we expressed C-terminally *Strep*-tagged
141 SpaO_{V203A} in a *spaO* knockout strain and purified it using *Strep*-Tactin affinity chromatography.
142 Interestingly, this mutation did not only almost completely abolish the production of soluble
143 SpaO_C, but also drastically reduced the levels of soluble full-length SpaO_{V203A} (Fig. 2A), which
144 instead formed insoluble inclusion bodies (data not shown). Complementation of the mutant with
145 *spaO_C* restored the soluble levels of both proteins, indicating that SpaO_C is required for SpaO
146 stability in solution.

147

148 The observed enhancement of SpaO solubility could involve interaction between SpaO and
149 SpaO_C, as reported for homologous proteins (18-20). Therefore, we used size-exclusion
150 chromatography (SEC) coupled to MALS and SAXS, as well as native MS to study complex
151 formation between the two SpaO isoforms. In native MS non-covalent complexes of biological
152 samples are ionized and transferred to the gas phase under mild conditions, making it a sensitive
153 technique to take a snapshot of all non-covalent assemblies in a sample (21-23). First, we
154 observed that SpaO_C exists mostly as a homodimer in solution (Fig. 2B and Fig. S3A, Table S4,
155 SASDC68), consistent with the crystal structure of the SPOA2-SPOA2 domain dimer of SpaO
156 and homolog proteins in *Shigella* and *Yersinia* (15,19,20). A very low abundance of
157 homotetramers was observed irrespective of the protein concentration tested (Fig. 2B), indicating
158 that these complexes reflect biologically relevant units and are not the result of unspecific
159 clustering during the MS ionization process.

160
161 Subsequent analysis of co-purified SpaO/SpaO_C showed that both proteins interact to form
162 predominantly heterotrimers with a stoichiometry of SpaO-2SpaO_C (Fig. 2C and Fig. S3B, Table
163 S4, SASDC78). Notably, no monomeric SpaO was detected in MS measurements, which
164 indicates high binding affinity within the SpaO-2SpaO_C complex and further highlights the
165 critical role of SpaO_C in SpaO solubility. Excess SpaO_C was found to be mainly dimeric,
166 suggesting that it binds to SpaO as a pre-formed dimer. In addition to the predominant SpaO-
167 2SpaO_C species, we also observed the dimerization of these heterotrimers into 2(SpaO-2SpaO_C)
168 heterohexamers, which was independent of both the protein concentrations and the position of the
169 *Strep*-tag (Fig. 2C, Fig. S3C). Higher-order oligomers could only be observed when measuring
170 highly concentrated samples that showed unspecific clustering during the ionization process and
171 were therefore considered to be non-specific assemblies. This conclusion is also supported by
172 SEC-MALS, which at a high protein concentration of 140 μM showed no evidence of species
173 larger than the 2(SpaO-2SpaO_C) heterohexamer (Fig. S3B). Selected ions of the SpaO-2SpaO_C
174 heterotrimers were subjected to collision-induced dissociation (CID) MS/MS experiments. The
175 observed dissociation pathways in these experiments give further insights into complex topology
176 since dissociating proteins are mostly small monomeric proteins from the periphery of protein
177 complexes, although the process of CID is not completely understood and exceptions have been
178 reported (24). Here, one SpaO_C monomer was found to dissociate, leaving a residual SpaO-
179 SpaO_C complex (Fig. 2C inset).

180

181 In order to determine the domain of interaction between SpaO and SpaO_C, we purified constructs
182 covering different regions of SpaO and combined them for native MS and SEC-MALS/SAXS
183 analysis (Table 1). By themselves, both the SpaO N-terminal domain (SpaO₁₋₁₄₅) and a construct
184 containing the SPOA1 and SPOA2 domains (SpaO₁₄₀₋₂₉₇) are mostly monomeric in solution (Fig.
185 S4A, Table S4, SASDC88 and SASDEK7). Combination of these proteins with SpaO_C in both
186 SEC-MALS/SAXS and native MS subsequently showed the formation of a stable
187 SpaO₁₋₁₄₅-2SpaO_C complex resembling the SpaO:2SpaO_C stoichiometry, while only very low
188 levels of complexes between SpaO_C and SpaO₁₄₀₋₂₉₇ could be detected (Fig. 3A-C, Fig. S4C, D,
189 Table S4 and SASDC98). We characterized the interaction between SpaO₁₋₁₄₅ and the SpaO_C
190 dimer by isothermal titration calorimetry (ITC) and obtained a K_d of $1.04 \pm 0.21 \mu\text{M}$, which also
191 demonstrates strong affinity between these proteins (Fig. 3D, E). Together, these results
192 demonstrate that the intermolecular interaction between the SpaO isoforms is mediated by SpaO_C
193 stably binding to the N-terminal domain of SpaO. Furthermore, no significant interaction was
194 detected between the N-terminal domain and the C-terminal SPOA1-SPOA2 domain dimer of
195 SpaO (Fig. 3C, Fig. S4B), indicating that in SpaO these domains are held together largely by
196 their covalent linkage, suggesting conformational flexibility between them.

197

198 **Sorting platform subcomplexes of SpaO_C, SpaO, OrgB and InvC are stable in solution.**

199 Next, we determined the interactions of SpaO and SpaO_C with other proteins of the *Salmonella*
200 sorting platform in solution by co-expression with the interaction partners OrgB and InvC (8) in
201 *E. coli* (Table 1). While OrgB by itself was insoluble (data not shown), stable complexes of
202 SpaO/SpaO_C/OrgB, SpaO/SpaO_C/OrgB/InvC and OrgB/InvC were soluble and could be purified
203 for further characterization (Fig. 4A). We also tested co-expression of these proteins with OrgA,
204 but this did not yield any soluble OrgA-containing complexes, suggesting that OrgA could either
205 require the presence of needle base-forming proteins for correct folding, or stay localized to the
206 membrane or needle base and not participate in soluble sorting platform complexes.

207 In order to determine the regions of OrgB involved in interactions with SpaO/SpaO_C and InvC,
208 we dissected OrgB into its N-terminal (residues 1-105) and C-terminal (residues 106-226) halves
209 and co-expressed His-tagged variants of these together with *Strep*-tagged InvC or SpaO/SpaO_C.
210 Subsequent *Strep*-Tactin affinity purification showed that OrgB₁₋₁₀₅ is pulled down by

211 SpaO/SpaO_C, while only trace amounts co-purified with InvC (Fig. 4B). Conversely, OrgB₁₀₆₋₂₂₆,
212 was pulled down by InvC, and even though small amounts could also be pulled down by
213 SpaO/SpaO_C, the ratio between SpaO/SpaO_C and OrgB₁₀₆₋₂₂₆ indicates that the affinity between
214 them is low. We similarly dissected InvC after residue 79 and tested the ability of *Strep*-tagged
215 InvC₁₋₇₉ and InvC₈₀₋₄₃₁ to pull down OrgB. While both full-length InvC and InvC₁₋₇₉ were able to
216 co-purify OrgB, this was not the case for InvC₈₀₋₄₃₁ (Fig. 4C), showing that the N-terminal 79
217 amino acids of InvC are both necessary and sufficient for its interaction with OrgB. Together,
218 these results show that OrgB interacts through its C-terminus with the N-terminal 79 amino acids
219 of InvC and confirm that the binding site for SpaO is located in the N-terminus of OrgB (15).

220
221 **OrgB dimers induce dimerization of SpaO-2SpaO_C.** We analyzed the SpaO/SpaO_C/OrgB
222 complex by native MS and found that the major molecular species contains two units of SpaO-
223 2SpaO_C bound to two molecules of OrgB, resulting in 2(SpaO-2SpaO_C)-2OrgB complexes. Less
224 abundant species, possibly representing assembly intermediates of this complex, were also
225 identified (Fig. 5). The vast majority of OrgB-containing complexes possesses two molecules of
226 OrgB, which indicates that OrgB exists mainly in dimeric form, similar to its flagellar homolog
227 FliH (25). When we subjected the 2(SpaO-2SpaO_C)-2OrgB species to MS/MS analysis, a single
228 OrgB dissociated from the complex, while a second, less prominent dissociation pathway led to
229 the dissociation of a SpaO monomer (Fig. S5A).

230
231 We also attempted native MS analysis of the mutant SpaO_{V203A}, in which the start codon of
232 SpaO_C has been mutated, both alone and in complex with OrgB. While it was possible to purify
233 both SpaO_{V203A} and SpaO_{V203A}/OrgB complexes lacking SpaO_C by affinity purification and SEC,
234 these complexes were unstable and could not be detected in native MS or successfully analyzed
235 by other methods. This highlights the importance of SpaO_C not only for the stability of SpaO, but
236 also of higher-order sorting platform complexes containing OrgB.

237
238 **The ATPase InvC binds to SpaO/SpaO_C/OrgB complexes to form the core building block of**
239 **the sorting platform.** The most comprehensive sorting platform subcomplexes we obtained in
240 this study contained the four proteins SpaO, SpaO_C, OrgB and InvC. Native MS revealed that the
241 ATPase InvC is present in different types of complexes, with species of SpaO-2SpaO_C-2OrgB-

242 InvC and 2(SpaO-2SpaO_C)-2OrgB-InvC stoichiometry being the most abundant in the spectra
243 (Fig. 6A). Complexes of 2OrgB-InvC and 2SpaO-2SpaO_C-2OrgB-InvC stoichiometry were
244 detected at lower levels. Importantly, InvC was detected exclusively in complexes containing
245 OrgB dimers, which is in agreement with our findings that the OrgB C-terminal region binds to
246 the N-terminus of InvC (Fig. 4B, C) and previously reported CET maps and pull-down assays
247 (10,15). It should be noted that the signal intensity ratios of the different complex species were
248 heavily dependent on the electrospray conditions and while the presented spectrum was selected
249 for a high resolution, the majority of acquired spectra showed higher signal intensities for high
250 molecular weight complexes. However, direct translation of signal intensity ratios into complex
251 ratios in solution is not possible due to fluctuating signals and different ionization and
252 transmission efficiencies of different complex species. Nevertheless, the different observed
253 species indicate a degree of dynamic association and dissociation of subunits within the system.
254 In addition to the species identified in the presented mass spectrum, occasionally signals in the
255 higher *m/z*-range were observed, depending on the electrospray conditions (Fig. S6). Due to the
256 low resolution and signal intensity, charge states for these peaks could not be unambiguously
257 identified in MS or MS/MS measurements. However, the mass range and peak interval suggest
258 the presence of complexes with masses of approximately 433 kDa, possibly dimers of 2(SpaO-
259 2SpaO_C)-2OrgB-InvC.

260 In CID MS/MS measurements of the different identified SpaO/SpaO_C/OrgB/InvC complexes the
261 dissociation of a single OrgB monomer was observed in every case (Fig. S5B, C). Because no
262 other components were lost together with the OrgB, this dissociation pattern allows us to
263 conclude that the interactions of the OrgB dimer with both SpaO/SpaO_C and InvC are mediated
264 by the same OrgB molecule, while the other is less tightly integrated in the complex.

265 We further characterized the SpaO/SpaO_C/OrgB/InvC complexes using SEC-MALS and SEC-
266 SAXS. MALS revealed a molecular mass range over the main SEC elution peak of
267 approximately 208 to 180 kDa (Fig. 6B), which is in good agreement with the complexes
268 identified in native MS (Table S3). Since this analysis showed the later regions of the elution
269 peak to be a mixture of several molecular species, we only used the largely homogenous first half
270 of the peak in the SAXS analysis in order to generate a model with minimal averaging between
271 different species. Subsequently, bead model reconstruction from the SAXS data showed that the
272 SpaO/SpaO_C/OrgB/InvC adopts an extended L-shape in solution. (Fig. 7A-C, Table S4,

273 SASDEJ7). By simultaneously employing the SAXS data of the SpaO/SpaO_C/OrgB/InvC and the
274 SpaO-2SpaO_C complexes in a multiphase bead modeling approach (26), the position of SpaO-
275 2SpaO_C within the larger complex could be determined. The resulting multiphase bead model
276 indicates that SpaO-2SpaO_C is located in the shorter leg of the extended L-shape (Fig. 7D).

277 Unfortunately, due to the complexity of the studied system the generation of a reliable SAXS-
278 based atomistic hybrid model of the SpaO/SpaO_C/OrgB/InvC complex is hindered by a number
279 of uncertainties, which include the number of different subunits, flexibility of the complex in
280 solution (indicated by Kratky analysis, see SASBDB), the remaining possibility of heterogeneity
281 in the SEC peak region used for SAXS analysis and a lack of high-resolution structure for many
282 of the complex components. Nevertheless, by combining the SpaO/SpaO_C/OrgB/InvC SAXS data
283 with our native MS results and the interactions between different subunit domains (Table 1), it is
284 possible to construct a schematic model of the architecture of the soluble
285 SpaO/SpaO_C/OrgB/InvC complex (Fig. 7E). Thus, while SpaO-2SpaO_C occupies the shorter leg
286 of the L-shape, InvC-OrgB would be placed in the longer leg with OrgB forming a linker
287 between SpaO-2SpaO_C and InvC. Interestingly, even though native MS and MALS indicate the
288 presence of two SpaO-2SpaO_C heterotrimers in the SpaO/SpaO_C/OrgB/InvC complex (Fig. 6,
289 Table S3), both the multiphase analysis (Fig. 7D) and comparison of the SpaO/SpaO_C and
290 SpaO/SpaO_C/OrgB/InvC SAXS bead structures (see SASBDB for details) indicate that only a
291 single SpaO-2SpaO_C heterotrimer can be accommodated in the short leg of the L-shape,
292 suggesting that the SAXS structure is that of a complex with SpaO-2SpaO_C-2OrgB-InvC
293 stoichiometry. This apparent discrepancy could be due to uncertainties in the SAXS bead model
294 caused by flexibility of the complex or heterogeneity in the SEC peak region used for SAXS
295 analysis.

296
297 Because the extended SAXS shape of the SpaO-2SpaO_C-2OrgB-InvC complex is reminiscent of
298 the pod densities seen in the *in-situ* 3D CET map of the *Salmonella* needle complex (10), we
299 hypothesized that this complex represents the soluble core building block from which the full
300 sorting platform is assembled. To test this hypothesis, we superimposed the *ab initio* SAXS bead
301 model with the CET map (Fig. 8), which shows a good correspondence between the two
302 structures and orients the SAXS shape in a way that places SpaO-2SpaO_C in the outer pods, InvC
303 in the central hub and 2OrgB in the linker region between the two. This is in good agreement

304 with the assignments by CET using fluorescent protein tags and sorting platform protein deletions
305 (10,27). If six units of the SAXS bead model were to be placed within the CET map, steric
306 clashes would occur in the central hub region. Interestingly, Kratky analysis of the SAXS data
307 showed conformational flexibility of the building block complexes, indicating an ability to
308 undergo conformational changes upon assembly of the complete sorting platform. In fact, by
309 rotating InvC in our model upwards by 90° around its interaction site with OrgB and shifting that
310 interaction site towards the bottom of the central hub, InvC would be re-oriented into a
311 configuration parallel to the outer pods with its C-terminus pointing towards the T3SS basal
312 body. This change would both resolve the steric clashes and allow for the formation of an InvC
313 ATPase hexamer to fill the central hub region of the CET map.

314 It should, however, be noted that this *in silico* approach relies on the superposition of two
315 structures of low resolution, both of which are associated with their own errors, posing a limit on
316 the conclusions that can be drawn from it. Therefore, while the good agreement between our
317 SAXS structure and the CET map supports our idea that the SpaO/SpaO_C/OrgB/InvC complex
318 represents the soluble core building block of the sorting platform, biochemical studies will be
319 required to show the assembly of these soluble complexes into the complete sorting platform.

320

321 **Discussion**

322

323 The sorting platform, together with the export apparatus complex, is still one of the less well
324 characterized components of the T3SS. In this work we present an analysis of inter-subunit
325 interactions, stoichiometry and shape of the main soluble module of the SPI-1 sorting platform in
326 *S. Typhimurium*. Expression and functional analysis confirm that the gene encoding the protein
327 SpaO produces an additional short protein SpaO_C that comprises the C-terminus of the SpaO
328 sequence, and that SpaO_{FL} is essential for type III secretion, while SpaO_C appears non-essential
329 but required for full secretion efficiency (16,17). Interestingly, a similar phenotype has been
330 observed for the *Salmonella* SPI-2 orthologue protein SsaQ_C (18) and the remaining secretion
331 activity upon deletion of the shorter protein product appears to be unique to the two T3SSs of
332 *Salmonella*. This raises the possibility that cross-complementation might occur between the
333 *Salmonella* T3SSs, a hypothesis that could be the subject of future investigations. On the other

334 hand, given that MALDI MS showed that low levels of a SpaO_C-like protein were still produced
335 from a *spaO* variant carrying a mutation in the SpaO_C start codon (*spaO*_{V203A}), it is possible that
336 the incomplete loss of secretion and invasion activity of the Δ *spaO*_C mutant might be due to
337 partial complementation by such a product that appears to be produced by proteolysis even in the
338 absence of internal translation initiation (Fig. 1B, C). Overall, these data are consistent with the
339 results of previous studies in the *Salmonella* SPI-1 and SPI-2 systems, as well as *Shigella* and
340 *Yersinia* (12,16-20), suggesting that the alternative translation into a full-length protein and a
341 shorter product may represent a widespread strategy among the SctQ proteins of virulence-
342 associated T3SSs.

343
344 The isoform SpaO_C forms a homodimer that binds to the full-length SpaO to form SpaO-2SpaO_C
345 complexes, similar to the 1:2 complexes observed for the *Shigella* Spa33 and the *Yersinia* YscQ
346 homologs (19,20). However, while the Spa33-2Spa33_C trimers readily assembled into higher-
347 order oligomers, we found only little dimerization of trimers and no further oligomerization for
348 SpaO-2SpaO_C. Additionally, our analysis shows that the SpaO_C dimer stably associates with the
349 N-terminal domain of SpaO (SpaO₁₋₁₄₅). In contrast, stable interactions between SpaO_C and the
350 SPOA domains of SpaO, like those observed for the homolog Spa33, could not be detected (20).
351 Interestingly, in a recent study a SpaO variant carrying a photo-activatable amino acid in the
352 SPOA2 domain (residue 289) was found to cross-link with SpaO_C, indicating interaction between
353 these regions after all (16). However, given the irreversibility of cross-linking and the
354 comparatively low levels of cross-linked species in that study, these might have been the result of
355 more transient interactions such as those indicated by the low levels of SpaO₁₄₀₋₂₉₇-SpaO_C
356 complexes observed in native MS (Fig. 3C). Importantly, our newly found stable interaction
357 between the N-terminal domain of SpaO and SpaO_C has implications for any model of the
358 structure of the T3SS cytosolic complex, which is currently based on interactions between the
359 small SctQ protein isoform and the SPOA1-SPOA2 domain dimer of the full-length variant.

360
361 The SpaO-2SpaO_C heterotrimer interacts with the ATPase regulator OrgB to form stable 2(SpaO-
362 2SpaO_C)-2OrgB complexes (Fig.5) and we therefore propose that OrgB exists as a dimer
363 comparable to its flagellar homolog FliH (25). Interestingly, while it has been suggested that the
364 binding of SpaO_C and OrgB to SpaO may be mutually exclusive due to overlapping binding sites
365 on the C-terminal SPOA1-SPOA2 domains of SpaO (15,16), our data shows that SpaO can

366 simultaneously interact with both of these proteins. This is consistent with our finding that SpaO_C
367 interacts with the N-terminal domain of SpaO rather than the C-terminal SPOA domains. In
368 addition, in CID MS/MS of 2(SpaO-2SpaO_C)-2OrgB complexes the dissociation of both SpaO
369 and OrgB monomers was observed, indicating that the recruitment of OrgB leads to a
370 stabilization of SpaO_C within the complex. While our data does not offer a clear mechanism for
371 this stabilization, it is conceivable that it involves direct interactions between SpaO_C and OrgB
372 that occur in addition to those of the extreme N-terminus of OrgB and the SpaO SPOA1-SPOA2
373 dimer (15). Furthermore, the dissociation of either OrgB or SpaO without the simultaneous loss
374 of other subunits suggests that direct interactions between the two SpaO-2SpaO_C trimers are
375 promoted in these complexes. It should be noted that the observed MS/MS dissociation pattern is
376 also compatible with a complex architecture in which both SpaO-2SpaO_C heterotrimers are
377 associated with the same OrgB unit. However, this arrangement seems unlikely since an
378 association of one SpaO-2SpaO_C trimer to one OrgB would be expected in light of the reported
379 interaction between the N-terminus of OrgB and the SPOA1-SPOA2 domains of SpaO (15).
380 Nevertheless, it cannot be excluded given the asymmetry of OrgB units within the OrgB dimer
381 revealed by MS/MS of SpaO/SpaO_C/OrgB/InvC complexes (see below).

382
383 Complexes of SpaO, SpaO_C and OrgB associate with the ATPase InvC to form both SpaO-
384 2SpaO_C-2OrgB-InvC and 2(SpaO-2SpaO_C)-2OrgB-InvC complexes, in which OrgB acts as a
385 central connector by binding of its N-terminus to SpaO-2SpaO_C and its C-terminus to InvC.
386 Based on MS/MS experiments (Fig. S5), we propose that both of these interactions are formed by
387 the same OrgB subunit, while the second OrgB is less tightly integrated in the complex, possibly
388 acting to stabilize extended helical regions in the first OrgB. SAXS analysis showed that the
389 SpaO/SpaO_C/OrgB/InvC complexes adopt an extended L-shaped structure in solution. Because
390 this conformation is in good agreement with the *in situ* cryo-electron tomography (CET) structure
391 of the *Salmonella* SPI-1 T3SS (10), we propose that the SpaO/SpaO_C/OrgB/InvC complexes
392 identified in this study represent the main soluble building blocks of the sorting platform. These
393 complexes would bind to other T3SS proteins like the docking protein OrgA, InvI or the export
394 apparatus and undergo a conformational change in re-orienting the ATPase InvC to assemble the
395 complete sorting platform at the base of the T3SS needle complex. Adding to the similarity of the
396 SAXS and CET structures the fact that we found SpaO_C in all of the sorting platform
397 subcomplexes, its importance for their stability and that SpaO_C is itself stabilized in these

398 complexes by the presence of OrgB, it can be hypothesized that SpaO_C is an integral structural
399 part of the sorting platform similar to the *Yersinia* homolog YscQ_C, which has previously been
400 shown to co-localize with YscQ_{FL} into sorting platform complexes at the bacterial membrane
401 (12). On the other hand, the *in vitro* nature of our study means that it cannot be excluded that
402 SpaO_C plays a role in the soluble forms of the building blocks and might dissociate from the
403 complexes upon assembly of the complete sorting platform *in vivo*, as has been suggested by the
404 lack of additional densities in CET maps of sorting platforms from strains expressing SpaO_C
405 fused to a fluorescent protein (16).

406
407 The superposition between our SAXS bead model and the CET map suggests that the individual
408 legs as seen by tomography would be of SpaO-2SpaO_C-2OrgB-InvC stoichiometry, bringing the
409 assembled sorting platform to 6SpaO-12SpaO_C-12OrgB-6InvC. While these numbers are
410 compatible with the stoichiometry determined by fluorescence microscopy for InvC and OrgB,
411 SpaO has been indicated to be present in the sorting platform at a higher copy number of
412 approximately 24 (13). Our findings show that the soluble building blocks can recruit an
413 additional SpaO-2SpaO_C trimer and it is conceivable that further units dynamically associate with
414 the sorting platform at the T3SS needle base. In fact, the dynamic exchange of the SpaO homolog
415 YscQ in *Yersinia* has previously been observed by fluorescence microscopy and found to
416 increase during the active secretion process (12). Together with the observation that the diffusion
417 behavior of cytosolic populations of sorting platform components also changes upon secretion
418 activation, this indicates that soluble sorting platform complexes might play an important role in
419 the function of type 3 secretion (28). Thus, it can be hypothesized that soluble building blocks of
420 SpaO/SpaO_C/OrgB/InvC could act as T3SS substrate shuttles that recruit substrate-chaperone
421 complexes in the cytosol and transfer them to the basal-body associated sorting platform for
422 subsequent secretion. Furthermore it can be speculated that the dissociation of SpaO/SpaO_C/OrgB
423 from hexameric T3SS-associated InvC might act to fully activate the secretion process by
424 overcoming the inhibitory effect of OrgB on InvC ATPase activity (25,29).

425

426 **Experimental Procedures**

427 **Cloning and mutagenesis of *Salmonella* genes.** Genes ligated into the expression vectors
428 pASK-IBA (IBA GmbH, Göttingen, Germany), pET (Novagen, Madison, WI, USA), or

429 pCDFDuet-1 (Novagen, Madison, WI, USA) were derived from *Salmonella* Typhimurium strain
430 SL1344 using standard techniques. All PCRs were performed using Phusion polymerase (New
431 England Biolabs, Ipswich, MA, USA) and oligonucleotides synthesized by Sigma-Aldrich or
432 Eurofins Genomics. Site-directed mutagenesis of the *spaO* gene was performed according to the
433 QuikChange PCR site-directed mutagenesis protocol (Agilent, Santa Clara, CA, USA). All
434 primers used in this study can be found in Table S5.

435
436 *Salmonella* genomic *spaO* deletion was carried out by homologous recombination using the λ
437 Red recombinase system (30). Briefly, the λ Red recombinase plasmid pKD46 was expressed in
438 *S. Typhimurium* SL1344 and a kanamycin cassette flanked by two 50bp regions homologous to
439 the *spaO* gene was subsequently transformed into the strain for homologous recombination. The
440 $\Delta spaO_C$, $\Delta spaO_{FL}$, *spaO*-3xFLAG, $\Delta spaO_C$ -3xFLAG and $\Delta spaO_{FL}$ -3xFLAG strains were
441 generated following a similar protocol, introducing a tetracycline cassette into the *spaO* region as
442 described above. In a second step, the tetracycline cassette was replaced by *spaO* DNA carrying
443 mutations and colonies were selected on tetracycline-sensitivity selection media (31,32). To
444 generate the $\Delta spaO_C$ strain, silent mutations at the internal putative Shine-Dalgarno region
445 (position 594 to 600, AGGGGGA to gGGcGGc) and start codon (position 607-609, GTG to GTt)
446 of *spaO* were introduced, while the $\Delta spaO_{FL}$ strain was produced by introducing nonsense
447 mutations shortly after the start codon of *spaO* at amino acid position 28 and 29. For the
448 generation of the strains *spaO*-3xFLAG, $\Delta spaO_C$ -3xFLAG and $\Delta spaO_{FL}$ -3xFLAG, a 3xFLAG-
449 tag was inserted at the C-terminus of *spaO* in the chromosome. Introduction of mutations was
450 verified by PCR and DNA sequencing. The $\Delta spi-1$ strain was kindly provided by the lab of
451 Arturo Zychlinsky.

452
453 **Detection of SpaO and SpaO_C in *Salmonella* cells.** *spaO*-3xFLAG, $\Delta spaO_C$ -3xFLAG and
454 $\Delta spaO_{FL}$ -3xFLAG strains were grown in LB medium (Luria/Miller) at 37 °C to an OD₆₀₀ of 1.
455 Total cell lysates were separated by SDS-PAGE and analyzed by western blot using anti-FLAG
456 M2 primary antibody (Sigma-Aldrich, St. Louis, MO, USA), horseradish peroxidase (HRP)-
457 conjugated secondary antibodies (Jackson ImmunoResearch Laboratories, West Grove, PA,
458 USA) and ECL western blotting substrates (Thermo Fischer Scientific, Waltham, MA, USA) for
459 protein detection.

460

461 **Recombinant gene expression and protein purification.** Constructs used for recombinant gene
462 expression in *E. coli* BL21 (DE3) are listed in Table S6. Cells were grown in LB with the
463 appropriate antibiotics at 37 °C. At an OD₆₀₀ of 0.5, the temperature was reduced to 20 °C and
464 gene expression induced by addition of 200 µg/l anhydrotetracycline (AHT, Sigma-Aldrich, St.
465 Louis, MO, USA) for pASK-IBA vectors and/or 0.5 mM IPTG for pET and pCDFDuet plasmids.
466 Cells were grown further for 18 h and harvested by centrifugation.

467

468 All purification steps were performed at 4 °C. To purify SpaO_C, SpaO₁₋₁₄₅, SpaO₁₄₀₋₂₉₇,
469 SpaO₁₋₁₄₅/SpaO_C, SpaO/SpaO_C, SpaO/SpaO_C/OrgB/InvC and OrgB/InvC complexes, cell pellets
470 were resuspended in buffer B1 (100 mM Tris pH 7.5, 150 mM NaCl) supplemented with
471 complete EDTA-free protease inhibitor cocktail (Roche), 1 mg/ml lysozyme, 10 µg/ml DNase I
472 and 2 mM 2-mercaptoethanol (2ME). Cell lysis was achieved by French press and lysates were
473 clarified by centrifugation at 48,000 x g for 30 min. The protein complexes were purified by
474 *Strep*-Tactin affinity chromatography and eluted with buffer B1 supplemented with 7.5 mM
475 desthiobiotin. Affinity-purified proteins were polished by size-exclusion chromatography (SEC)
476 on Superdex 75 or Superdex 200 columns (GE Healthcare, Chicago, IL, USA) equilibrated with
477 buffer B2 (20 mM HEPES pH 7.5, 350 mM NaCl). The affinity-purified OrgB/InvC and
478 SpaO/SpaO_C/OrgB/InvC complexes were further purified by SEC on a Superose 6 column
479 equilibrated with 10 mM Tris-HCl pH 8.0, 50 mM NaCl, with InvC/OrgB having been dialyzed
480 against the same buffer before the SEC. For SpaO/SpaO_C/OrgB complex purification, cells were
481 resuspended in buffer B3 (20 mM sodium phosphate buffer pH 7.4, 500 mM NaCl) supplemented
482 with 40 mM imidazole, protease inhibitors, 1 mg/ml lysozyme, 10 µg/ml DNase I and 2 mM
483 2ME. The SpaO/SpaO_C/OrgB complex was immobilized on HisTrap HP columns (GE
484 Healthcare, Chicago, IL, USA), washed with buffer B3 containing 3 mM ATP and 10 mM MgCl₂
485 and eluted with buffer B3 containing 400 mM imidazole. Eluted proteins were diluted three-fold
486 in buffer B1, purified by *Strep*-Tactin affinity chromatography, followed by SEC in a Superdex
487 200 column equilibrated with buffer B2.

488

489 For solubility analysis of sorting platform proteins (Table S6), cells were lysed by sonication
490 (Sonopuls HD 2070, Bandelin, Berlin, Germany), soluble and insoluble fractions were separated
491 by centrifugation and analyzed by SDS-PAGE and western blot using anti-*Strep* (Qiagen, Hilden,

492 Germany) and anti-His (GE Healthcare, Chicago, IL, USA) primary antibodies, HRP-conjugated
493 secondary antibodies and SuperSignal West Dura Extended Duration Substrate (Thermo Fisher
494 Scientific, Waltham, MA, USA) for detection.

495 For the purification of OrgB fragments with SpaO/SpaO_C and InvC, as well as InvC fragments
496 with OrgB, cells were resuspended in buffer B1 supplemented with complete EDTA-free
497 protease inhibitor cocktail (Roche, Basel, Switzerland), 1 mg/ml lysozyme, 10 µg/ml DNase I,
498 2 mM 2-ME and 1 mM MgCl₂. Cells were lysed by sonication, lysates clarified by centrifugation
499 and protein from the soluble fraction purified by *Strep*-Tactin affinity purification. Eluted
500 proteins were analyzed by SDS-PAGE followed by Coomassie-staining or western blot using an
501 anti-His primary antibody (Thermo Fisher Scientific, Waltham, MA, USA), HRP-conjugated
502 secondary antibody (Jackson ImmunoResearch Laboratories, West Grove, PA, USA) and
503 ClarityMax ECL substrate (Bio-Rad, Hercules, CA, USA).

504 To test the effect of SpaO_C on the solubility of mutant SpaO proteins, plasmid constructs (Table
505 S6) were expressed for 3 h at 37 °C in a *Salmonella spaO*-knockout strain (SL1344Δ*spaO*).
506 Harvested cells were resuspended in phosphate-buffered saline and lysed with BugBuster reagent
507 (Novagen, Madison, WI, USA). Soluble proteins were loaded onto *Strep*-Tactin resin and loaded
508 resin was analyzed by SDS-PAGE and Coomassie staining.

509
510 **Protein secretion.** Strains were grown in LB at 37 °C for 6 h to induce SPI-1 effector protein
511 secretion. Where appropriate, expression was induced with AHT at an OD₆₀₀ of 0.1. Proteins
512 were precipitated from 12-13 ml of filtered culture supernatants by addition of 15% ice-cold
513 trichloroacetic acid (TCA) and centrifugation at 3.200 x g for 90 min. Pellets were washed with
514 ice-cold acetone, air-dried and resuspended in 200 mM Tris-HCl (pH 8.0) containing 200 mM
515 NaCl. Samples were loaded onto SDS-PAGE gels and analyzed by Coomassie staining and
516 western blot. Rabbit anti-SipB, anti-SipC, anti-SipD and anti-SopB polyclonal antibodies were
517 raised and applied for detection of T3SS-dependent substrates in western blot analysis. Anti-FliC
518 (kindly provided by Marc Erhardt's lab) and anti-DnaK antibodies (Stressgen Biotechnologies,
519 San Diego, CA, USA) were used as loading control and lysis control, respectively. HRP-
520 conjugated secondary antibodies and ECL western blotting substrates were used for protein
521 detection.

522
523 **Invasion assay.** The murine epithelial cell line MODE-K (33) was cultivated in Dulbecco's
524 modified Eagle's medium (DMEM). 5×10^5 cells were seeded in 24-well plates and infected with
525 *Salmonella* strains at a multiplicity of infection (MOI) of 10 for 1 h at 37 °C with 5% CO₂ in a
526 humidified tissue culture incubator. After treating the cells with 100 µg/ml gentamycin for 1 h,
527 cells were washed with sterile PBS three times. Infected monolayers were lysed with 1 % Triton-
528 X and colony forming units (CFU) were determined by serial dilution and plating. Relative
529 invasion of each strain was calculated by comparison of the CFUs after invasion with those of the
530 inoculum.

531
532 **Isothermal titration calorimetry (ITC).** ITC of SpaO_C binding to the SpaO₁₋₁₄₅ was performed
533 using a MicroCal VP-ITC titration calorimeter (Malvern Panalytical, Almelo, Netherlands)
534 calibrated to 25°C. 1.4 ml of SpaO₁₋₁₄₅ at 8 µM was placed in the sample cell, and the syringe
535 was loaded with 120 µM of SpaO_C dimer. Injections of 10 µl were performed with stirring at 310
536 rpm and the heat of reaction was recorded. Data were analyzed using Origin (OriginLab,
537 Northampton, MA, USA).

538
539 **Native mass spectrometry.** Purified protein samples were buffer-exchanged into 50 mM
540 ammonium acetate pH 7.5 (SpaO and SpaO fragments), 300 mM ammonium acetate pH 7.5
541 (SpaO_C/SpaO/OrgB) or 50 mM ammonium acetate pH 8 (SpaO/SpaO_C/OrgB/InvC) using
542 Vivaspin® 500 centrifugal concentrators (Sartorius, Göttingen, Germany). SEC-purified proteins
543 were used for all samples but the SpaO/SpaO_C/OrgB complex, which was affinity-purified.
544 Samples were loaded into home-made gold-coated glass capillaries (34), which were mounted
545 into the nano electrospray ionization (ESI) source of a QToF 2 mass spectrometer (Waters,
546 Manchester, UK, and MS Vision, Almere, the Netherlands) adapted for high-mass experiments
547 (35) and operated in positive ion mode. Capillary and cone voltages of 1.3 to 1.5 kV and 110 to
548 150 V were applied, respectively. The source pressure was set in the range of 6 to 10 mbar and
549 argon was used as collision gas at 1.7 to 1.9 x 10⁻² mbar. Acceleration voltages for collision-
550 induced dissociation (CID) were optimized for resolution and minimal complex dissociation. CID
551 tandem mass spectrometry (MS/MS) experiments on protein complexes were performed to
552 confirm mass assignments and deduce topological information by selecting specific precursor

553 peaks for dissociation and ramping acceleration voltages up to 400 V or until the entire precursor
554 signal disappeared. Cesium iodide spectra (25 mg/ml) were acquired on the same day of each
555 measurement and used to calibrate raw data using MassLynx software (Waters, Manchester, UK).
556 Peak series were assigned with MassLynx and Massign (36). Average measured masses of
557 protein complexes, standard deviations of replicate measurements and average full width at half
558 maximum (FWHM) values as a measure of the mass heterogeneity and resolution are listed in
559 Table S3.

560

561 **Small-angle X-ray scattering and multi-angle light scattering.** Small-angle X-ray scattering
562 (SAXS) measurements were carried out at the beamline P12 (EMBL/DESY, Hamburg, Germany)
563 (37) at the PETRA III storage ring using a Pilatus 2M detector (Dectris, Baden-Dätwil,
564 Switzerland). The SAXS camera was set to a sample-detector distance of 3.1 m, covering the
565 momentum transfer range $0.008 \text{ \AA}^{-1} < s < 0.47 \text{ \AA}^{-1}$ $s = 4\pi \sin(\theta)/\lambda$ (where 2θ is the scattering
566 angle and $\lambda=1.24 \text{ \AA}$ is the X-ray wavelength). For each SAXS measurement, 75-90 μl of affinity-
567 purified protein sample was loaded onto a Superdex 200 Increase 10/300 GL SEC column (GE
568 Healthcare, Chicago, IL, USA) previously equilibrated with 20 mM HEPES pH 7.5, 150 mM
569 NaCl and eluted at 0.5 ml/min. In the case of the SpaO/SpaO_C/OrgB/InvC complex, Superose 6
570 10/300 GL (GE Healthcare, Chicago, IL, USA) equilibrated with 10 mM Tris-HCl pH 8.0, 50
571 mM NaCl and a flow rate of 0.3 ml/min was used. The sample eluting from the SEC column was
572 split into two fractions using a mobile phase-flow splitter. One fraction was directed to the SAXS
573 flow cell and the other into a triple detector array of UV absorption, multi-angle light scattering
574 (MALS, Wyatt MiniDawn Treos), and RI detectors (Wyatt Optilab T-rEX, both Wyatt, Santa
575 Barbara, CA, USA). Only in the case of SpaO/SpaO_C/OrgB/InvC, independent experiments were
576 run for SAXS and MALS data acquisition. The molecular masses of the separated sample
577 components eluting from the column were estimated by combining the results from light and X-
578 ray scattering with RI and UV absorption measurements. For each sample the scattering profiles
579 over the elution peak, collected with an exposure time of 1 s each, were separated into sample
580 and buffer regions, appropriately averaged and the signal from the buffer was subtracted using
581 CHROMIXS (38).

582

19

583 **SAXS model-free parameters.** The radius of gyration R_g and forward scattering intensity $I(0)$
584 were determined using Guinier analysis (39) and an indirect Fourier transformation approach by
585 the program GNOM (40), the latter also providing maximum particle dimensions D_{max} .
586

587 **Structural modelling against SAXS data.** *Ab initio* models were reconstructed from the
588 scattering data using bead modelling program DAMMIF and multiphase modelling program
589 MONSA (26,41). Ten independent reconstructions were averaged to generate a representative
590 model with the program DAMAVER (42). The average DAMMIF model was also used to
591 calculate the excluded volume of the particle, V_{DAM} , from which an independent MW estimate
592 can be derived (empirically, $MM_{DAM} \sim V_{DAM}/2$). Resolutions of the *ab initio* models were
593 computed using a Fourier Shell Correlation (FSC) based approach (43). Ambiguity associated
594 with spherically averaged single-particle scattering was determined using by AMBIMETER (44).
595

596 For the comparison between SAXS data and the electron microscopy density map the program
597 Chimera (45) was used to superimpose a bead model based on the *ab initio* SAXS shape with the
598 *Salmonella* T3SS CET map (EMDB ID: EMD-8544). A contour level of 2.53 was used for the
599 CET.

600 **Accession Codes.** The details of the SAXS analysis and the generated models were deposited at
601 the Small-Angle Scattering Biological Data Bank (SASBDB) under the codes: SASDC68
602 (SpaO_C); SASDEK7 (SPA0₁₄₀₋₂₉₇); SASDC88 (SpaO₁₋₁₄₅); SASDC98 (SpaO₁₋₁₄₅/SpaO_C);
603 SASDC78 (SpaO/SpaO_C); SASDEJ7 (SpaO/SpaO_C/OrgB/InvC).
604
605

606 **Acknowledgements**

607 The authors gratefully acknowledge P. Jungblut and M. Schmidt for the MALDI-TOF/TOF mass
608 spectrometry analysis, B. Jaschok-Kentner and W. Blankenfeldt for Edman sequencing, C.
609 Jeffries for the MALS analysis, M. Lunelli for CET and SAXS alignment and J. de Diego for her
610 useful comments and critical reading of the manuscript.
611

612 This work was funded by the European Research Council under the European Community's
613 Seventh Framework Programme (FP7/2007–2013). The Heinrich Pette Institute, Leibniz Institute
614 for Experimental Virology is supported by the Free and Hanseatic City of Hamburg and the
615 German Federal Ministry of Health. JH and CU are funded by the Leibniz Association through
616 SAW-2014-HPI-4 grant. AT was supported by the EMBL interdisciplinary Postdoc Programme
617 under Marie Curie COFUND Actions.

618

619 **Conflicts of Interest**

620 The authors declare that they have no conflicts of interest with the contents of this article.

621

622

623

624 **References**

- 625 1. Hueck, C. J. (1998). Type III protein secretion systems in bacterial pathogens of animals and
626 plants. *Microbiol. Mol. Biol. Rev.* 62, 379-433.
- 627 2. Coburn, B., Sekirov, I., Finlay, B. B. (2007). Type III secretion systems and disease. *Clin. Microbiol.*
628 *Rev.* 20, 535-549.
- 629 3. Dohlich, K., Zumsteg, A. B., Goosmann, C., Kolbe, M. (2014). A substrate-fusion protein is trapped
630 inside the type III secretion system channel in *Shigella flexneri*. *PLoS Pathog.* 10, e1003881.
- 631 4. Radics, J., Königsmaier, L., Marlovits, T. C. (2014). Structure of a pathogenic type 3 secretion
632 system in action. *Nat. Struct. Mol. Biol.* 21, 82-87.
- 633 5. Galan, J. E., Lara-Tejero, M., Marlovits, T. C., Wagner, S. (2014). Bacterial type III secretion
634 systems: specialized nanomachines for protein delivery into target cells. *Annu. Rev. Microbiol.*
635 68, 415-438.
- 636 6. Deane, J. E., Abrusci, P., Johnson, S., Lea, S. M. (2010). Timing is everything: the regulation of
637 type III secretion. *Cell. Mol. Life Sci.* 67, 1065-1075.
- 638 7. Barison, N., Gupta, R., Kolbe, M. (2013). A sophisticated multi-step secretion mechanism: how
639 the type 3 secretion system is regulated. *Cell. Microbiol.* 15, 1809-1817.
- 640 8. Lara-Tejero, M., Kato, J., Wagner, S., Liu, X., Galan, J. E. (2011). A sorting platform determines the
641 order of protein secretion in bacterial type III systems. *Science* 331, 1188-1191.
- 642 9. Morita-Ishihara, T., Ogawa, M., Sagara, H., Yoshida, M., Katayama, E., Sasakawa, C. (2006).
643 *Shigella* Spa33 is an essential C-ring component of type III secretion machinery. *J. Biol. Chem.*
644 281, 599-607.
- 645 10. Hu, B., Lara-Tejero, M., Kong, Q., Galan, J. E., Liu, J. (2017). In situ molecular architecture of the
646 *Salmonella* type III secretion machine. *Cell* 168, 1065-1074 e1010.
- 647 11. Makino, F., Shen, D., Kajimura, N., Kawamoto, A., Pissaridou, P., Oswin, H., Pain, M., Murillo, I.,
648 Namba, K., Blocker, A. J. (2016). The architecture of the cytoplasmic region of type III secretion
649 systems. *Sci. Rep.* 6, 33341.
- 650 12. Diepold, A., Kudryashev, M., Delalez, N. J., Berry, R. M., Armitage, J. P. (2015). Composition,
651 formation, and regulation of the cytosolic C-ring, a dynamic component of the type III secretion
652 injectisome. *PLoS Biol.* 13, e1002039.

- 653 13. Zhang, Y., Lara-Tejero, M., Bewersdorf, J., Galan, J. E. (2017). Visualization and characterization
654 of individual type III protein secretion machines in live bacteria. *Proc. Natl. Acad. Sci. USA* 114,
655 6098-6103.
- 656 14. Diepold, A., Sezgin, E., Huseyin, M., Mortimer, T., Eggeling, C., Armitage, J. P. (2017). A dynamic
657 and adaptive network of cytosolic interactions governs protein export by the T3SS injectisome.
658 *Nat. Commun.* 8, 15940.
- 659 15. Notti, R. Q., Bhattacharya, S., Lilic, M., Stebbins, C. E. (2015). A common assembly module in
660 injectisome and flagellar type III secretion sorting platforms. *Nat. Commun.* 6, 7125.
- 661 16. Lara-Tejero, M., Qin, Z., Hu, B., Butan, C., Liu, J., Galan, J. E. (2019). Role of SpaO in the assembly
662 of the sorting platform of a *Salmonella* type III secretion system. *PLoS Pathog.* 15, e1007565.
- 663 17. Song, M., Sukovich, D. J., Ciccarelli, L., Mayr, J., Fernandez-Rodriguez, J., Mirsky, E. A., Tucker, A.
664 C., Gordon, D. B., Marlovits, T. C., Voigt, C. A. (2017). Control of type III protein secretion using a
665 minimal genetic system. *Nat. Commun.* 8, 14737.
- 666 18. Yu, X. J., Liu, M., Matthews, S., Holden, D. W. (2011). Tandem translation generates a chaperone
667 for the *Salmonella* type III secretion system protein SsaQ. *J. Biol. Chem.* 286, 36098-36107.
- 668 19. Bzymek, K. P., Hamaoka, B. Y., Ghosh, P. (2012). Two translation products of *Yersinia yscQ*
669 assemble to form a complex essential to type III secretion. *Biochemistry* 51, 1669-1677.
- 670 20. McDowell, M. A., Marcoux, J., McVicker, G., Johnson, S., Fong, Y. H., Stevens, R., Bowman, L. A.,
671 Degiacomi, M. T., Yan, J., Wise, A., Friede, M. E., Benesch, J. L., Deane, J. E., Tang, C. M.,
672 Robinson, C. V., Lea, S. M. (2016). Characterisation of *Shigella* Spa33 and *Thermotoga* FliM/N
673 reveals a new model for C-ring assembly in T3SS. *Mol. Microbiol.* 99, 749-766.
- 674 21. Lossl, P., van de Waterbeemd, M., Heck, A. J. (2016). The diverse and expanding role of mass
675 spectrometry in structural and molecular biology. *EMBO J.* 35, 2634-2657.
- 676 22. Sharon, M. (2010). How far can we go with structural mass spectrometry of protein complexes?
677 *J. Am. Soc. Mass Spectrom.* 21, 487-500.
- 678 23. Ngounou Wetie, A. G., Sokolowska, I., Woods, A. G., Roy, U., Loo, J. A., Darie, C. C. (2013).
679 Investigation of stable and transient protein-protein interactions: Past, present, and future.
680 *Proteomics* 13, 538-557.
- 681 24. Benesch, J. L. P. (2009). Collisional Activation of Protein Complexes: Picking Up the Pieces. *J. Am.*
682 *Soc. Mass Spectrom.* 20, 341-348.
- 683 25. Minamino, T., MacNab, R. M. (2000). FliH, a soluble component of the type III flagellar export
684 apparatus of *Salmonella*, forms a complex with FliI and inhibits its ATPase activity. *Mol.*
685 *Microbiol.* 37, 1494-1503.
- 686 26. Svergun, D. I. (1999). Restoring low resolution structure of biological macromolecules from
687 solution scattering using simulated annealing. *Biophys. J.* 76, 2879-2886.
- 688 27. Hu, B., Morado, D. R., Margolin, W., Rohde, J. R., Arizmendi, O., Picking, W. L., Picking, W. D., Liu,
689 J. (2015). Visualization of the type III secretion sorting platform of *Shigella flexneri*. *Proc. Natl.*
690 *Acad. Sci. USA* 112, 1047-1052.
- 691 28. Rocha, J. M., Richardson, C. J., Zhang, M., Darch, C. M., Cai, E., Diepold, A., Gahlmann, A. (2018).
692 Single-molecule tracking in live *Yersinia enterocolitica* reveals distinct cytosolic complexes of
693 injectisome subunits. *Integr. Biol.* 10, 502-515.
- 694 29. Case, H. B., Dickenson, N. E. (2018). MxiN differentially regulates monomeric and oligomeric
695 species of the *Shigella* type three secretion system ATPase Spa47. *Biochemistry* 57, 2266-2277.
- 696 30. Datsenko, K. A., Wanner, B. L. (2000). One-step inactivation of chromosomal genes in *Escherichia*
697 *coli* K-12 using PCR products. *Proc. Natl. Acad. Sci. USA* 97, 6640-6645.
- 698 31. Bochner, B. R., Huang, H. C., Schieven, G. L., Ames, B. N. (1980). Positive selection for loss of
699 tetracycline resistance. *J. Bacteriol.* 143, 926-933.

- 700 32. Maloy, S. R., Nunn, W. D. (1981). Selection for loss of tetracycline resistance by *Escherichia coli*. J.
701 Bacteriol. 145, 1110-1111.
- 702 33. Vidal, K., Grosjean, I., evillard, J. P., Gespach, C., Kaiserlian, D. (1993). immortalization of mouse
703 intestinal epithelial cells by the SV40-large T gene. Phenotypic and immune characterization of
704 the MODE-K cell line. J. Immunol. Methods 166, 63-73.
- 705 34. Dunne, M., Leicht, S., Krichel, B., Mertens, H. D., Thompson, A., Krijgsveld, J., Svergun, D. I.,
706 Gomez-Torres, N., Garde, S., Uetrecht, C., Narbad, A., Mayer, M. J., Meijers, R. (2016). Crystal
707 structure of the CTP1L endolysin reveals how its activity is regulated by a secondary translation
708 product. J. Biol. Chem. 291, 4882-4893.
- 709 35. van den Heuvel, R. H., van Duijn, E., Mazon, H., Synowsky, S. A., Lorenzen, K., Versluis, C., Brouns,
710 S. J., Langridge, D., van der Oost, J., Hoyes, J., Heck, A. J. (2006). Improving the performance of a
711 quadrupole time-of-flight instrument for macromolecular mass spectrometry. Anal. Chem. 78,
712 7473-7483.
- 713 36. Morgner, N., Robinson, C. V. (2012). Massign: an assignment strategy for maximizing information
714 from the mass spectra of heterogeneous protein assemblies. Anal. Chem. 84, 2939-2948.
- 715 37. Blanchet, C. E., Spilotros, A., Schwemmer, F., Graewert, M. A., Kikhney, A., Jeffries, C. M., Franke,
716 D., Mark, D., Zengerle, R., Cipriani, F., Fiedler, S., Roessle, M., Svergun, D. I. (2015). Versatile
717 sample environments and automation for biological solution X-ray scattering experiments at the
718 P12 beamline (PETRA III, DESY). J. Appl. Crystallogr. 48, 431-443.
- 719 38. Franke, D., Petoukhov, M. V., Konarev, P. V., Panjkovich, A., Tuukkanen, A., Mertens, H. D. T.,
720 Kikhney, A. G., Hajizadeh, N. R., Franklin, J. M., Jeffries, C. M., Svergun, D. I. (2017). ATSAS 2.8: a
721 comprehensive data analysis suite for small-angle scattering from macromolecular solutions. J.
722 Appl. Crystallogr. 50, 1212-1225.
- 723 39. Guinier, A. (1939). La diffraction des rayons X aux très petits angles : application à l'étude de
724 phénomènes ultramicroscopiques. Ann. Phys. (Paris) 11, 161-237.
- 725 40. Svergun, D. I. (1992). Determination of the regularization parameter in indirect-transform
726 methods using perceptual criteria. J. Appl. Crystallogr. 25, 495-503.
- 727 41. Franke, D., Svergun, D. I. (2009). DAMMIF, a program for rapid ab-initio shape determination in
728 small-angle scattering. J. Appl. Crystallogr. 42, 342-346.
- 729 42. Volkov, V. V., Svergun, D. I. (2003). Uniqueness of ab initio shape determination in small-angle
730 scattering. J. Appl. Crystallogr. 36, 860-864.
- 731 43. Tuukkanen, A. T., Kleywegt, G. J., Svergun, D. I. (2016). Resolution of ab initio shapes determined
732 from small-angle scattering. IUCrJ 3, 440-447.
- 733 44. Petoukhov, M. V., Svergun, D. I. (2015). Ambiguity assessment of small-angle scattering curves
734 from monodisperse systems. Acta Crystallogr. D Biol. Crystallogr. 71, 1051-1058.
- 735 45. Pettersen, E. F., Goddard, T. D., Huang, C. C., Couch, G. S., Greenblatt, D. M., Meng, E. C., Ferrin,
736 T. E. (2004). UCSF Chimera - a visualization system for exploratory research and analysis. J.
737 Comput. Chem. 25, 1605-1612.

738

739 **Figure legends**

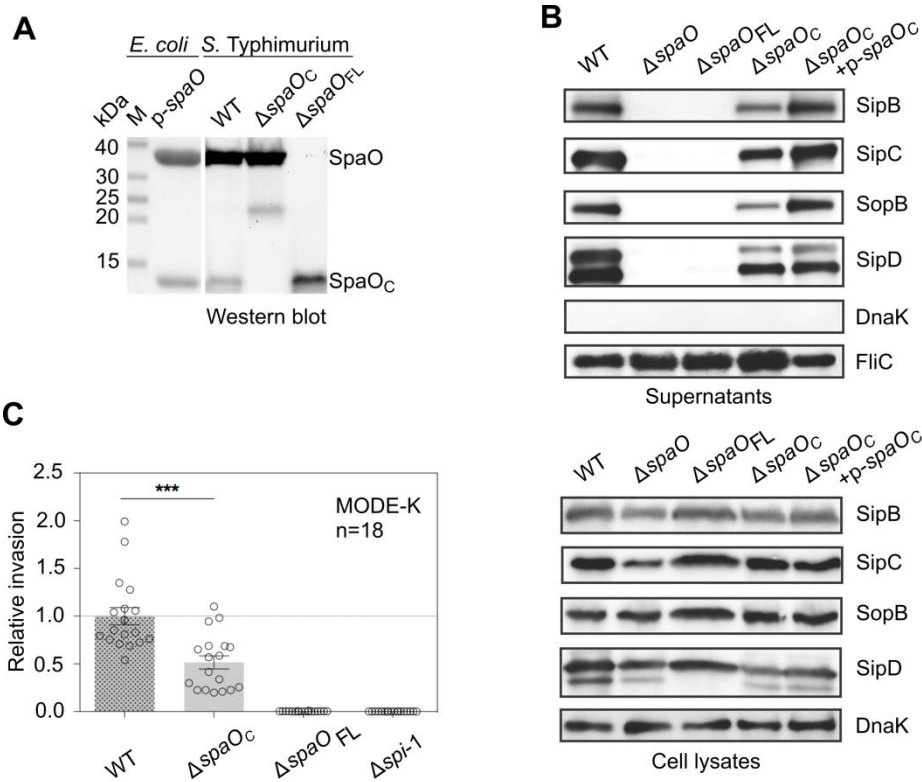
740 **Table 1.** Summary of interacting proteins and domains and complex stoichiometries.

Interactions	Pull down	Native MS	SEC-MALS	ITC	
SpaO/SpaOc	+	1:2 (2:4)	1:2 (2:4)	ND	741
SpaO _{V203A} / SpaOc	+	ND	ND	ND	742
SpaO _C /SpaOc	ND	1:1 (2:2, 4:4)	1:1	ND	743
SpaO ₁₋₁₄₅ /SpaOc	+	1:2 (1:4)	1:2	Kd = 1.04 ± 0.21 μM	
SpaO ₁₋₁₄₅ / SpaO ₁₄₀₋₂₉₇	ND	-	-	ND	744
SpaO ₁₄₀₋₂₉₇ /SpaOc	ND	(1:2)	-	ND	
SpaO/SpaOc /OrgB	+	2:4:2 (1:2:2, 1:2:1)	ND	ND	745
SpaO/SpaOc/OrgB ₁₋₁₀₅	+	ND	ND	ND	
SpaO/SpaOc/OrgB ₁₀₆₋₂₂₆	+/-	ND	ND	ND	746
SpaO _{V203A} /OrgB	+	Not stable	ND	ND	
OrgB/InvC	+	Not stable	ND	ND	747
OrgB ₁₋₁₀₅ /InvC	+/-	ND	ND	ND	
OrgB ₁₀₆₋₂₂₆ /InvC	+	ND	ND	ND	748
OrgB/InvC ₁₋₇₉	+	ND	ND	ND	
OrgB/InvC ₈₀₋₄₃₁	-	ND	ND	ND	749
SpaO/SpaOc/OrgB/InvC	+	1:2:2:1, 2:4:2:1 (2:2:2:1)	2:4:2:1	ND	

750 Alternative complexes detected by native mass spectrometry (MS) and SEC-MALS are indicated in
 751 brackets. ND= Not determined.

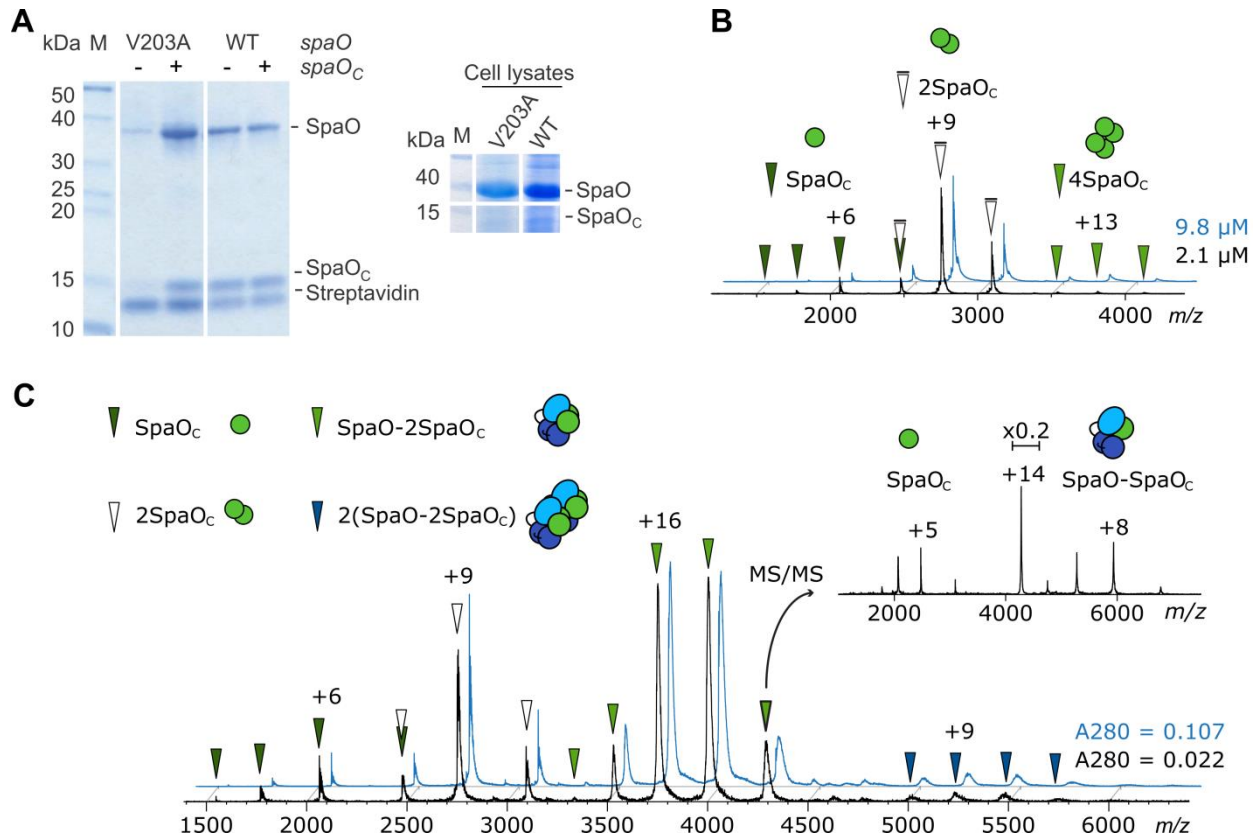
752

753



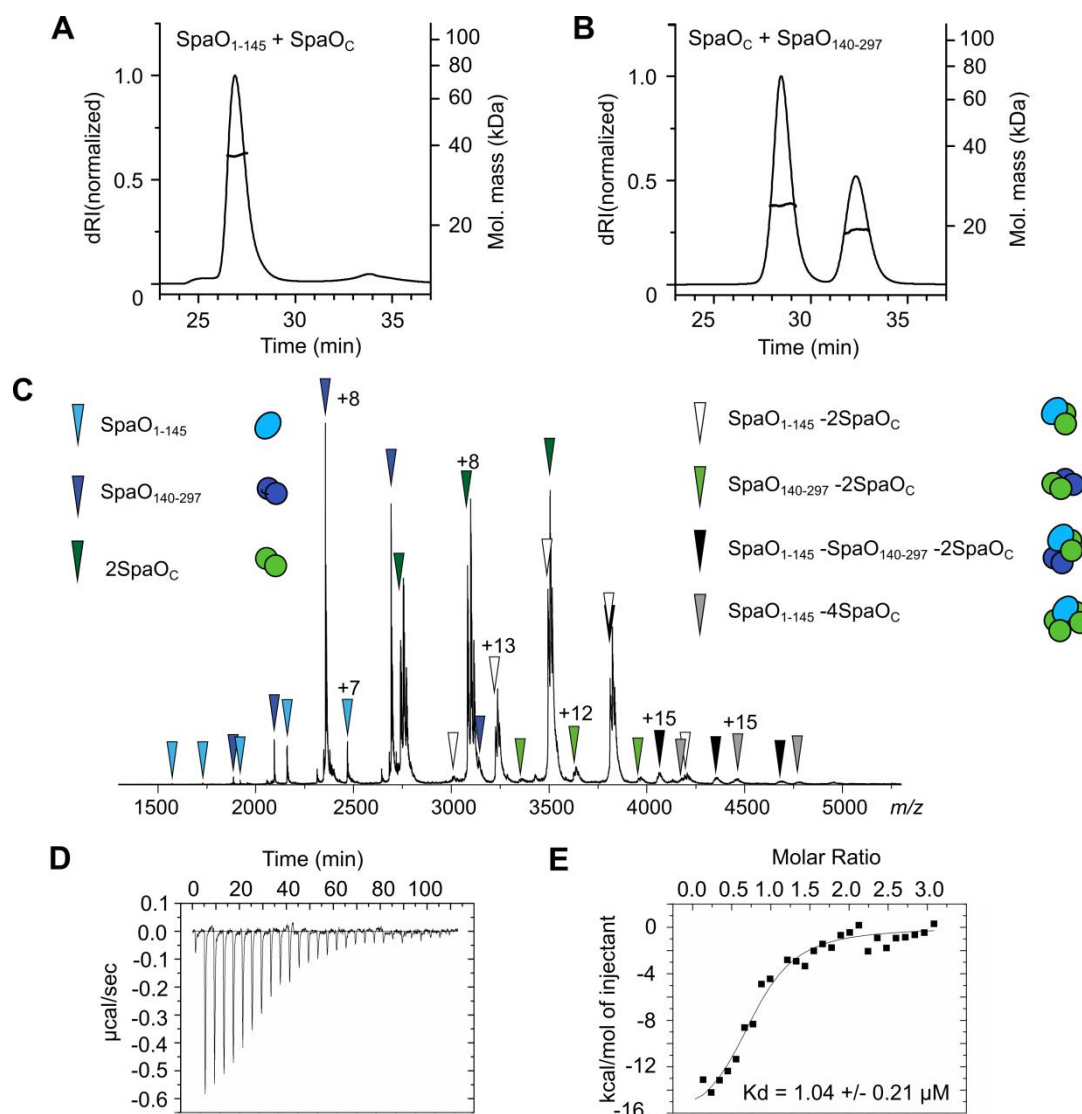
754

755 **Figure 1.** SpaOc is made by internal translation initiation within the *spaO* gene and is required
 756 for fully efficient T3 secretion. (A) Coomassie-stained SDS-PAGE of *Strep*-tagged SpaO and
 757 SpaOc purified from *E. coli* recombinantly expressing *spaO-Strep* (p-*spaO*) (left panel). Western
 758 blot detection of C-terminally 3xFLAG-tagged SpaO and SpaOc in whole cell lysates of
 759 *Salmonella* wild type (WT) and strains harboring silent mutations at the *spaO* internal Shine-
 760 Dalgarno sequence and start codon (Δ *spaOc*) or a nonsense mutation shortly after the *spaO* start
 761 codon (Δ *spaOFL*) (right panel). Molecular weight markers (M) are indicated and the result shown
 762 is representative of three biological replicates. (B) Western blot analysis of proteins secreted by
 763 *Salmonella* into culture supernatants (top panel). The proteins DnaK and FliC served as cell lysis
 764 control and loading control, respectively. Expression of T3SS substrates in whole cell lysates is
 765 shown in the bottom panel. Data shown are representative of three biological replicates. (C)
 766 Analysis of *Salmonella* invasion into MODE-K cells. Relative invasion was normalized to the
 767 levels of the wildtype and the results summarize three independent experiments. A *Salmonella*
 768 strain from which the entire *Salmonella* pathogenicity island 1 that encodes the SPI-1 T3SS has
 769 been deleted was included as a non-invasive control (Δ *spi-1*). Error bars represent one standard
 770 deviation. ***= p-value < 0.001

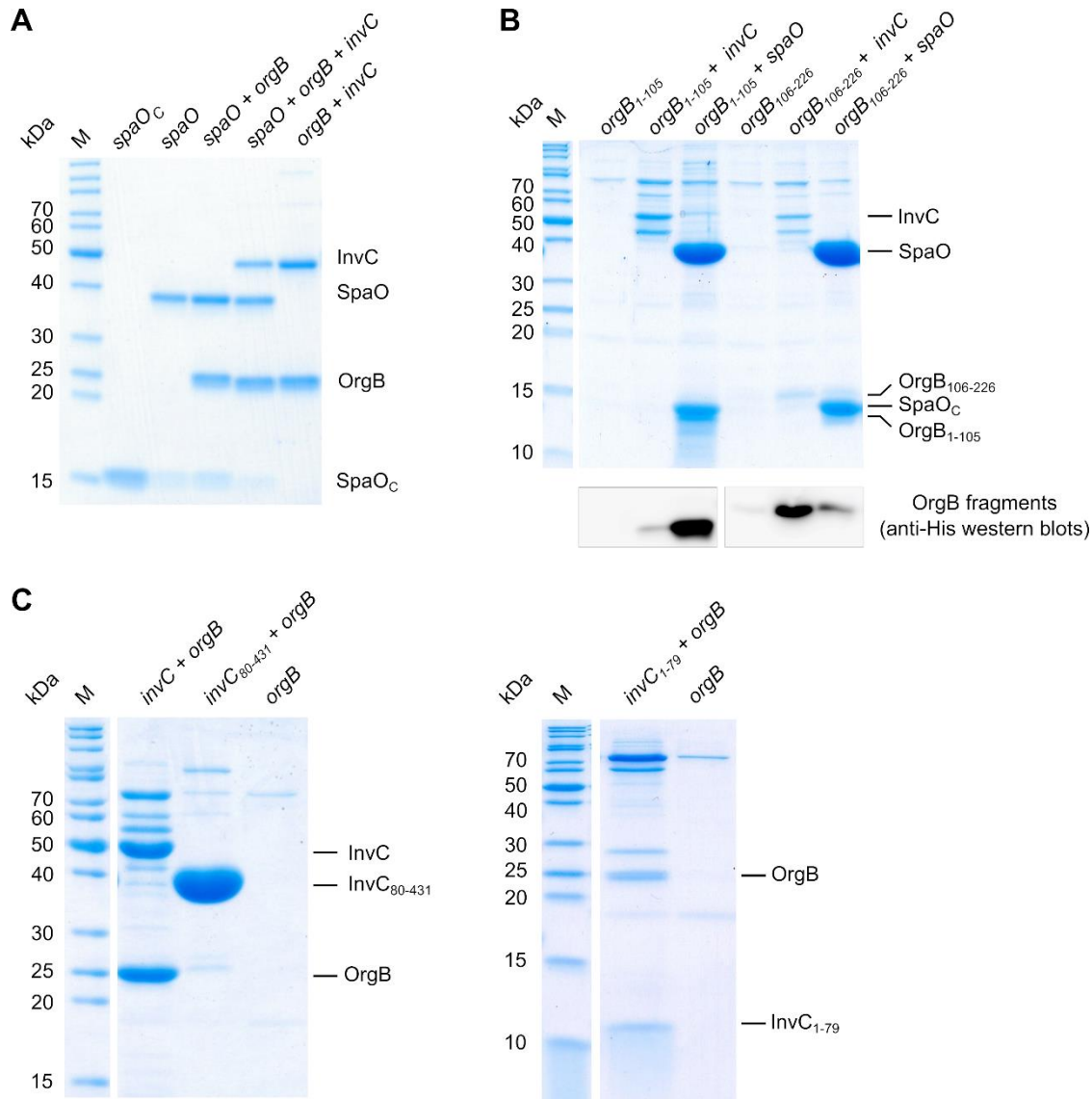


771

772 **Figure 2.** SpaO and SpaO_C interact to form stable 1:2 complexes. (A) Coomassie-stained SDS-
 773 PAGE of plasmid-encoded SpaO expressed in *Salmonella ΔspaO* and affinity-purified using
 774 *Strep*-Tactin. The SpaO V203A strain has a mutation at the SpaO_C start codon. The solubility of
 775 SpaO for the mutants was recovered by co-expression with plasmid-encoded *spaO_C* (+). A
 776 Coomassie-stained SDS-PAGE of whole cells lysates showing expression levels for SpaO and
 777 SpaO_C is depicted in the right panel. Molecular mass markers are included in lane M. (B) Native
 778 mass spectrum of SpaO_C at two different protein concentrations (black and blue spectra). SpaO_C
 779 monomers (dark green arrows), dimers (white arrows) and tetramers (light green arrows) are
 780 indicated. The main charge state of each protein or protein complex is labeled. (C) Native mass
 781 spectrum of SpaO/SpaO_C complexes at two different protein concentrations (black and blue
 782 spectra). The formation of SpaO-2SpaO_C complexes (light green arrows) and further dimerization
 783 of these heterotrimers (dark blue arrows) was observed irrespective of the protein concentration
 784 (indicated by absorbance at 280 nm, A₂₈₀). CID MS/MS (inset) of the +14 precursor of the
 785 heterotrimer shows dissociation of SpaO_C monomers and a residual SpaO-SpaO_C complex. Both
 786 SpaO and SpaO_C carry a C-terminal *Strep*-tag. The precursor peak in the MS/MS spectrum has
 787 been scaled down to 20% of its original size. Experimental and theoretical molecular masses are
 788 given in Table S3.



789
 790 **Figure 3.** Analysis of inter- and intramolecular domain interactions in SpaO-2SpaOC. (A) SEC-
 791 MALS analysis of co-purified SpaO₁₋₁₄₅/SpaO_C. SEC elution profiles (dRI traces) and the weight-
 792 averaged molar masses across the elution peaks are shown. The experimental mass is consistent
 793 with the formation of SpaO₁₋₁₄₅-2SpaO_C complexes (theoretical mass of 42kDa). (B) SEC-MALS
 794 analysis of combined SpaO₁₄₀₋₂₉₇ and SpaO_C. (C) Analysis of interactions between SpaO domains
 795 by native MS of mixed SpaO₁₋₁₄₅, SpaO₁₄₀₋₂₉₇ and SpaO_C. Besides monomeric components,
 796 SpaO₁₋₁₄₅-2SpaO_C heterotrimers (white arrows) were found. Other species like SpaO₁₋₁₄₅-
 797 2SpaO_C-SpaO₁₄₀₋₂₉₇ heterotetramers (black arrows), SpaO₁₋₁₄₅-4SpaO_C (grey arrows) and
 798 2SpaO_C-SpaO₁₄₀₋₂₉₇ (light green arrows) were detected at very low levels. The used SpaO_C
 799 sample comprised two protein species with a difference of about 131 Da, resulting in a
 800 characteristic peak fine structure with three distinct maxima for complex species containing 2
 801 SpaO_C. Native mass spectra of SpaO_C mixed with only SpaO₁₋₁₄₅ or SpaO₁₄₀₋₂₉₇ can be found in
 802 Fig. S4C and D. Experimental and theoretical molecular masses are given in Table S3. (D)
 803 Analysis of SpaO_C and SpaO₁₋₁₄₅ interaction by isothermal titration calorimetry (ITC). Raw heat
 804 signal for 10 μl injections of SpaO_C dimer (120 μM) to 1.4 ml of SpaO₁₋₁₄₅ (8 μM). (E) ITC
 805 integrated heats and fits to a 1:1 binding model where SpaO_C is considered a dimer. Data shown
 806 is representative of two experiments.



807
808
809 **Figure 4.** OrgB interacts with SpaO and InvC to form stable sorting platform subcomplexes
810 (A) Coomassie-stained SDS-PAGE of sorting platform proteins co-expressed in *E. coli* and
811 purified by affinity purification and size-exclusion chromatography. Co-expressed genes are
812 indicated above the gel, molecular mass markers are included in lane M. Affinity purification was
813 achieved by use of C-terminal *Strep*-tags for *spaO_C* and *spaO*, and a C-terminal *Strep*-tag on
814 InvC for *spaO+orgB+invC* and *orgB+invC*. In the case of *spaO+orgB* affinity purification
815 involved two steps using both a C-terminal His-tag on OrgB and a C-terminal *Strep*-tag on
816 SpaO/SpaO_C. (B) Top: Coomassie-stained SDS-PAGE of OrgB fragments co-expressed with
817 *Strep*-tagged *invC* or *spaO* in *E. coli* and purified by *Strep*-Tactin affinity purification. Bottom:
818 detection of the His-tagged OrgB fragments by western blot. (C) Coomassie-stained SDS-PAGEs
819 of *Strep*-tagged InvC fragments co-expressed with OrgB and purified by *Strep*-Tactin affinity
820 purification.

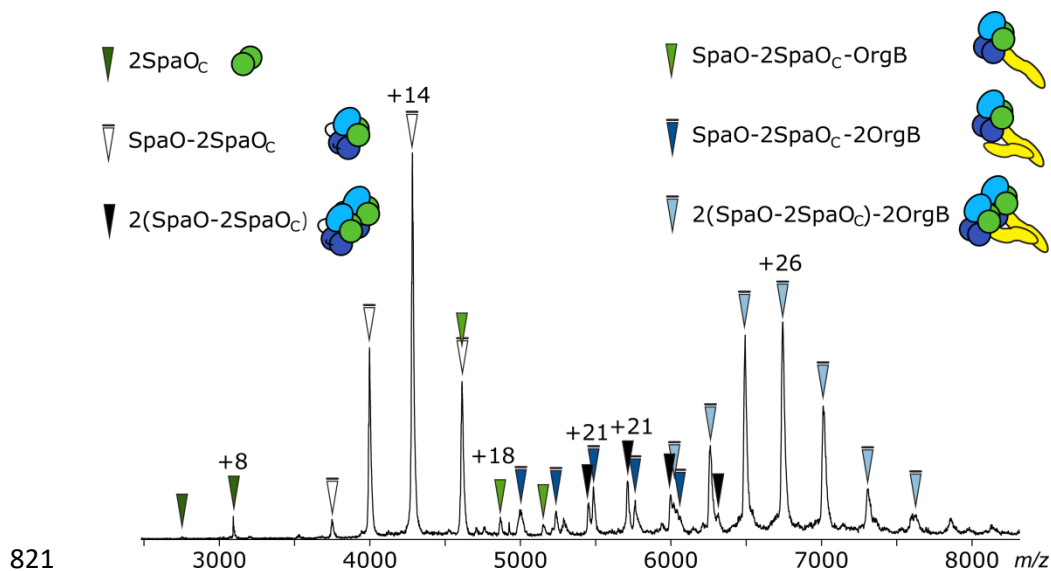
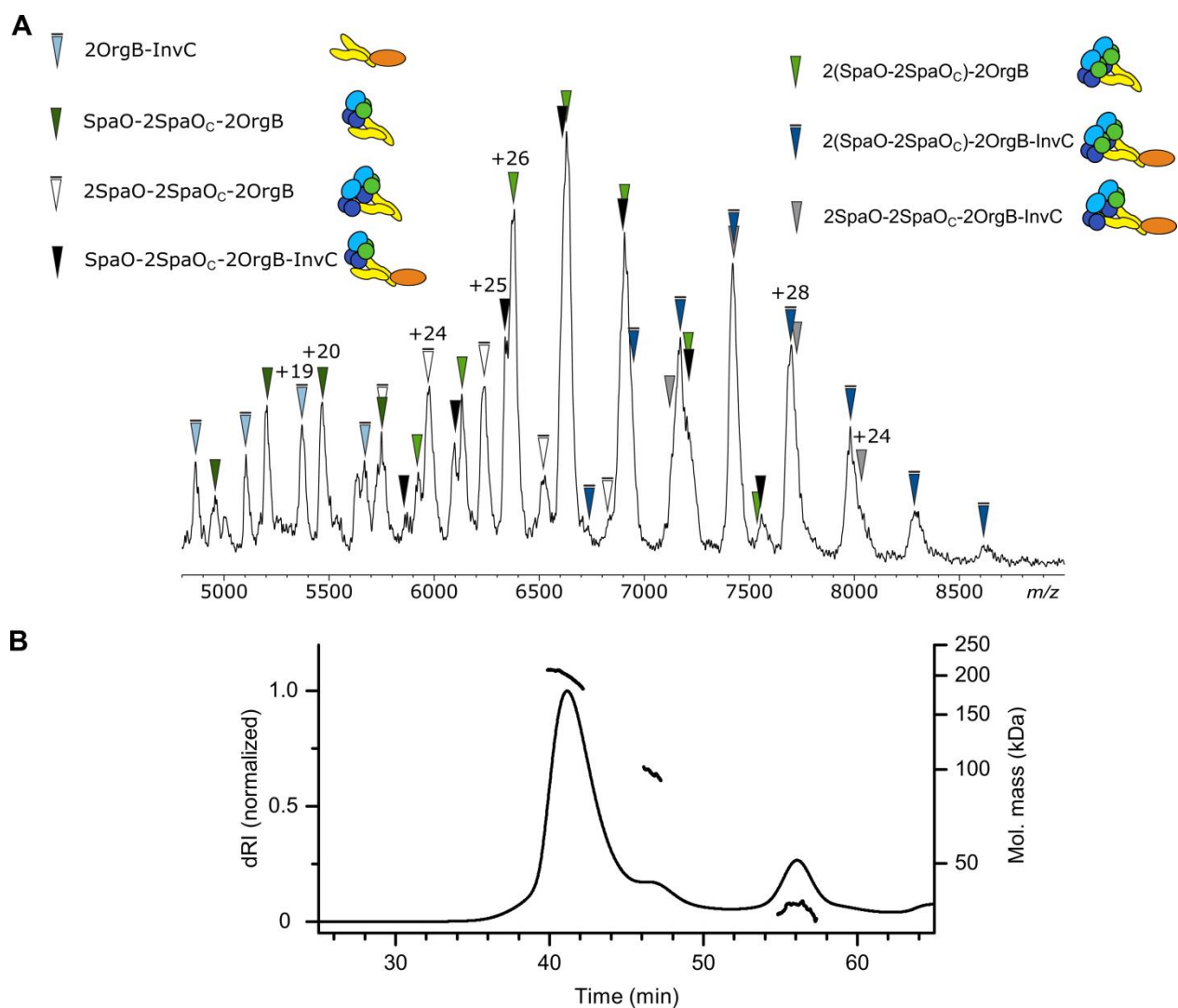
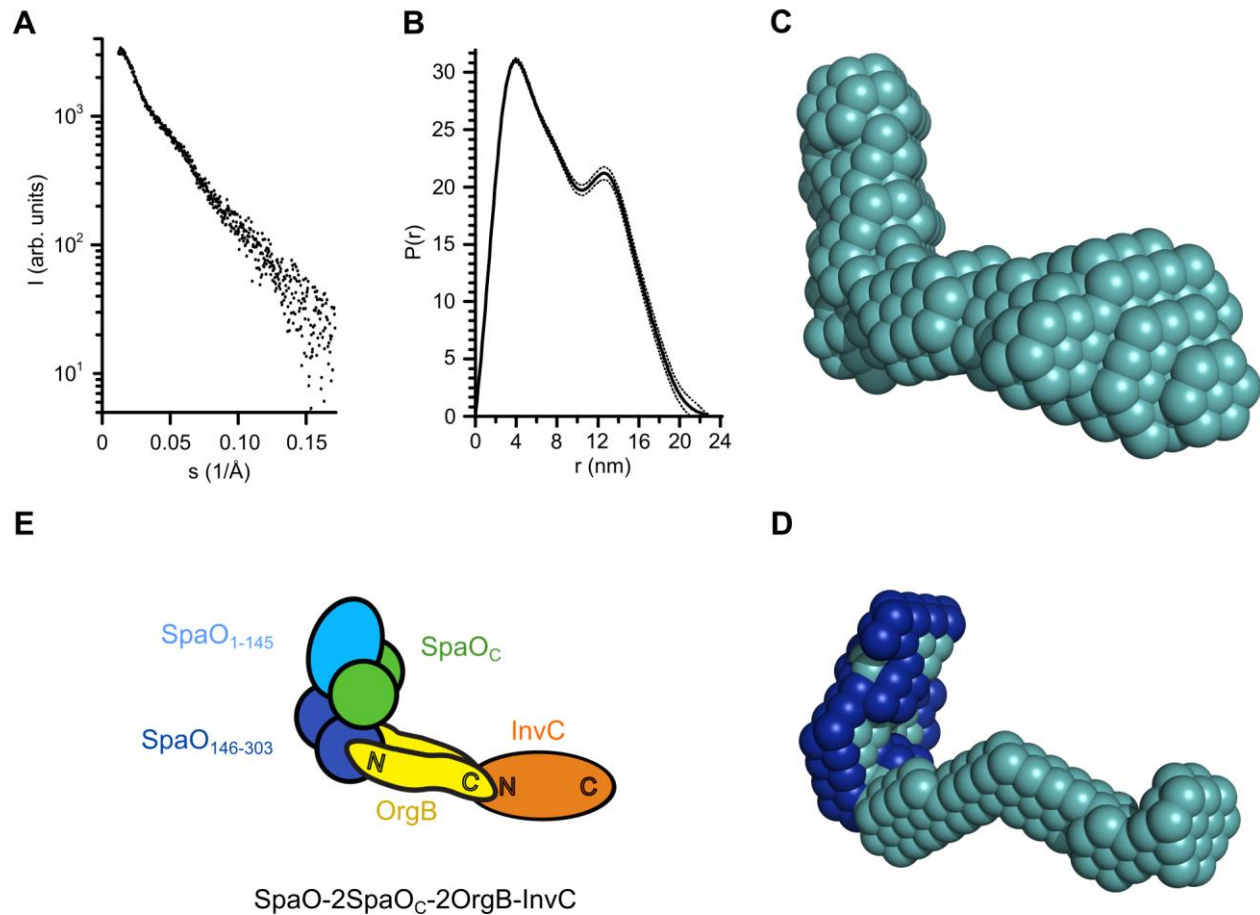


Figure 5. Native mass spectrum of SpaO/SpaOC/OrgB complexes. SpaO-2SpaOC heterotrimers (white arrows) bind to OrgB dimers resulting in 2(SpaO-2SpaOC)-2OrgB complexes (light blue arrows). 2(SpaO-2SpaOC) heterohexamers (black arrows) and a small fraction of SpaO-2SpaOC complexes bound to OrgB monomers (light green arrows) and dimers (dark blue arrows) were also observed. Experimental and theoretical molecular masses are given in Table S3.



828
829 **Figure 6.** The ATPase InvC binds to SpaO/SpaO_C/OrgB complexes. (A) Native mass spectrometry
830 of SpaO/SpaO_C/OrgB/InvC complexes. InvC-containing complexes of 2OrgB-InvC (light blue
831 arrows) SpaO-2SpaO_C-2OrgB-InvC (black arrows), 2(SpaO-2SpaO_C)-2OrgB-InvC (dark blue
832 arrows) and 2SpaO-2SpaO_C-2OrgB-InvC (grey arrows) are observed. Experimental and
833 theoretical molecular masses are given in Table S3. (B) SEC-MALS analysis of
834 SpaO/SpaO_C/OrgB/InvC complexes. SEC elution profiles (dRI traces) and the weight-averaged
835 molar masses across the elution peaks are shown.

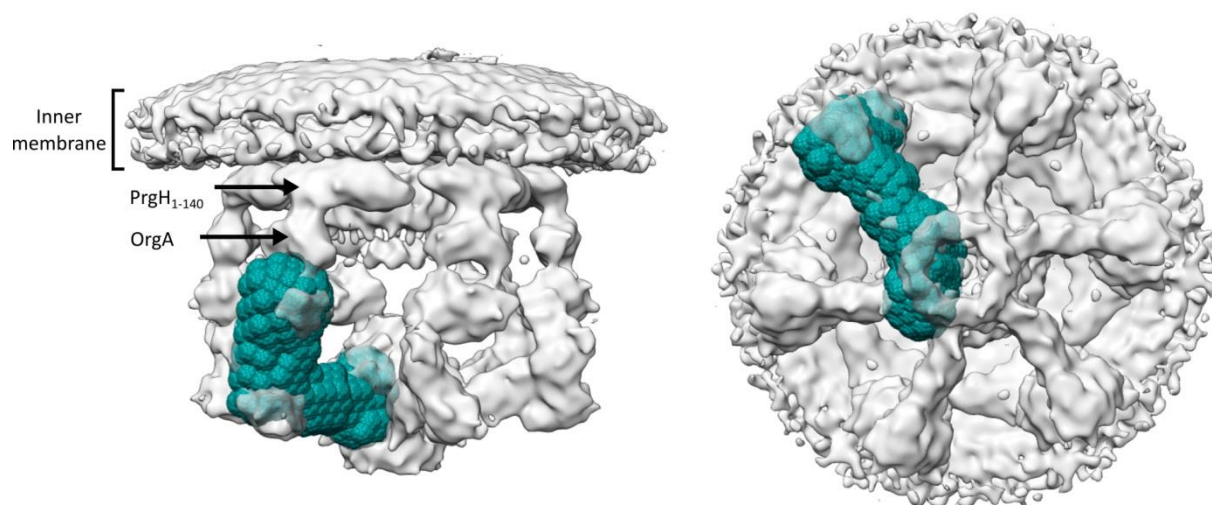


836

SpaO-2SpaO_C-2OrgB-InvC

837 **Figure 7.** Analysis of SpaO/SpaO_C/OrgB/InvC complexes by small-angle X-ray scattering. (A)
838 Small-angle X-ray scattering profile of SpaO/SpaO_C/OrgB/InvC. (B) Pair-distance distribution
839 function $P(r)$ computed from the SAXS data (A). (C) SAXS-based *ab initio* bead model of
840 SpaO/SpaO_C/OrgB/InvC. (D) MONSA multi-phase modeling using SAXS data of both of
841 SpaO/SpaO_C/OrgB/InvC and SpaO/SpaO_C. The phase corresponding to SpaO/SpaO_C is colored
842 dark blue. (E) Schematic model of the SpaO/SpaO_C/OrgB/InvC complex taking into account the
843 association of SpaO_C with the SpaO N-terminal domain SpaO₁₋₁₄₅ (Fig. 3), the interaction
844 between the SpaO SPOA1-SPOA2 dimer and the N-terminus of OrgB (15), and the interaction
845 between the C-terminal domain of OrgB and the N-terminal domain of InvC (Fig. 4B, C).

846



847

848 **Figure 8.** Superposition of the SAXS-based bead model (cyan) with the *in-situ* CET structure of
849 the *Salmonella* Typhimurium sorting platform (EMDB ID: EMD-8544, grey). Shown are a side
850 view (left) and bottom view (right). The N-terminal domain of PrgH (PrgH₁₋₁₄₀) and OrgA are
851 labeled according to Hu et al., 2017 (10).

852